Enhanced strength in pure Ti via design of alternating coarse- and fine-grain layers

Li, Danyang; Fan, Guohua; Huang, Xiaoxu; Juul Jensen, Dorte; Miao, Kesong; Xu, Chao; Geng, Lin; Zhang, Yubin; Yu, Tianbo

Published in:
Acta Materialia

Link to article, DOI:
10.1016/j.actamat.2021.116627

Publication date:
2021

Document Version
Publisher's PDF, also known as Version of record

Acta Materialia 206 (2021) 116627

Contents lists available at ScienceDirect

Acta Materialia

journal homepage: www.elsevier.com/locate/actamat

Enhanced strength in pure Ti via design of alternating coarse- and fine-grain layers

Danyang Li[a,c], Guohua Fan[b,*], Xiaoxu Huang[c,d,e], Dorte Juul Jensen[c], Kesong Miao[a], Chao Xu[a], Lin Geng[a,*], Yubin Zhang[c], Tianbo Yu[c,*]

[a] Department of Materials Science and Engineering, Harbin Institute of Technology, Harbin 150001, PR China
[b] Key Laboratory for Light-weight Materials, Nanjing Tech University, Nanjing 211816, PR China
[c] Department of Mechanical Engineering, Technical University of Denmark, Kgs. Lyngby DK-2800, Denmark
[d] International Joint Laboratory for Light Alloys (MOE), Department of Materials Science and Engineering, Chongqing University, Chongqing 400044, PR China
[e] Shenyang National Laboratory for Material Science, Chongqing University, Chongqing 400044, PR China

ARTICLE INFO

Article history:
Received 1 December 2020
Revised 3 January 2021
Accepted 4 January 2021
Available online 8 January 2021

Keywords:
Interface constraint
Multilayers
Yield strength
Dislocation
Titanium

ABSTRACT

The yield strength of metals is typically governed by the average grain size through the Hall-Petch relation, and it usually follows the rule of mixture (ROM) for layered composite materials. In the present study, an extraordinarily high yield strength, far beyond the predicted values from the Hall-Petch relation and the ROM, is achieved in a specially designed layered titanium that is characterized by alternating coarse- and fine-grain layers (C/F-Ti) where the grain sizes match the layer thicknesses in both the coarse- and fine-grained layers. The strengthening mechanism of such a layered C/F-Ti is investigated based on detailed experimental characterizations, including nanoindentation tests of local hardness, in-situ synchrotron Laue X-ray microdiffraction (μXRD) measurement of the lattice strain distribution during tensile testing, and transmission electron microscopy (TEM) analysis of the dislocation structure after yielding. In the coarse-grain layers, significantly higher hardness values are observed next to the layer interfaces compared to the layer center regions, and <c+a> dislocations and densely populated pile-ups of <a> dislocations are exclusively observed in the interface regions after yielding. These experimental results point to an enhanced interface constraint effect on the deformation mechanism in hexagonal close-packed (hcp) materials with a large difference in the critical resolved shear stress between <a> slip and <c+a> slip. The C/F-Ti combines the strength of fine grains and the ductility of coarse grains, demonstrating a new structural design strategy for property optimization of single-phase hcp materials.

1. Introduction

Metals as unique structural materials may be strengthened by alloying, which typically depends on nonrenewable resources and also makes recycling difficult [1,2]. Alloying, like most other strengthening mechanisms, may also lead to loss of ductility—referred to as strength-ductility trade-off [3–5]. Therefore, development of new strategies for designing long-term sustainable structural materials with a good combination of strength and ductility are highly demanded. Such a development requires effective control of the crystallographic defects including vacancies, dislocations and grain/phase boundaries, and this is a grand challenge due to the instability of these crystallographic defects during processing and application. In recent decades, the configurational design of materials provides a new opportunity to attack this challenge [1,6,7].

A layered structure as one of the configurational designs for materials exhibits its potential in improving strength and ductility simultaneously [8–15]. However, the underlying deformation mechanisms of layered materials have not been sufficiently understood. In the previous work, the deformation mechanism of Ti/Al layered metal composite (LMC), with a yield strength matching the rule of mixture (ROM) [16,17] and a ductility exceeding those of both components (Ti and Al sheets), was investigated [10,18]. The stress and deformation microstructure evolutions in that LMC were studied by in-situ neutron diffraction and differential aperture X-ray microscopy (DAXM), respectively. It was reported that the stress partitioning and strain-transfer during the early deformation stage influence the whole deformation process of the LMC

* Corresponding authors.
E-mail addresses: ghfan@njtech.edu.cn (G. Fan), genglin@hit.edu.cn (L. Geng), tiyu@mek.dtu.dk (T. Yu).

https://doi.org/10.1016/j.actamat.2021.116627
1359-6454/

significantly. However, the process of the early deformation stage is influenced by many factors: the differences in thermal expansion coefficient, elastic modulus and yield strength between Ti and Al, as well as the grain size and crystal orientation. Meanwhile, the large difference between two components leads to the nucleation of cracks appearing at a low tensile strain, in both the interfacial $TiAl_3$ layers and Al layers. Therefore, the constraint of the propagation of cracks by the layered structure also plays a vital role during plastic deformation. As a result, it is difficult to clarify how each factor exerts influence on the mechanical properties of the materials with layered structures. In this work, in order to investigate the influence of different yield strength in component layers on the mechanical properties of LMCs, excluding the influence of other factors mentioned above, layered titanium with alternating coarse- and fine-grain layers (C/F-Ti) was fabricated. The yield strength difference between the neighboring layers is expected to be controlled by grain size following the Hall-Petch relationship, while the other factors can be neglected since the layers are of the same material (i.e. Ti). From the perspective of the material we used, the unique deformation mechanism of Ti with hexagonal close-packed (hcp) crystal structure should also be taken into consideration during the design of C/F-Ti and the investigation of its deformation mechanism. The slip modes, the large variation of the critical resolved shear stress (CRSS), the anisotropy of elastic modulus and thermal expansion coefficient, and the unique texture of titanium provide further possibilities for the configurational design.

In titanium, <a> (<1-210>) slip on prismatic {10-10}, basal {0001} and pyramidal {10-11} planes can provide a maximum of four independent slip systems at ambient temperature [19–23]. Nevertheless, according to the von Mises criterion, five independent shear systems are required to accommodate an arbitrary plastic strain [24]. Therefore, <c+a> (<2-1-1-3>) slip on pyramidal {10-11}/{2-1-12} planes (pyr1/pyr2 <c+a> slip) and/or twinning are also needed in the deformation of polycrystalline titanium. Prismatic slip is the easiest slip system to be activated whereas pyramidal <c+a> slip and twinning are the most difficult among them due to the significant difference of CRSS [25–30], which has been measured by high energy X-ray diffraction microscopy (HEDM) [31]. The activation of slip systems is also orientation-dependent [32–35]. It is reported that one or more of the three prismatic slip systems are easy to be activated when grains are oriented with their c-axes nearly perpendicular to the applied uniaxial stress (owing to the high Schmid factors), which is called “soft grains”. “Hard grains” which have their c-axes nearly parallel to the applied stress often activate pyramidal <c+a> slip and deformation twinning to accommodate local strains during deformation due to the very low Schmid factor of prismatic slip [27,34,36–38]. Grain-grain interaction also plays an important role in the activation and transfer of dislocations, influencing mechanical properties [27,36,39–41]. Over the years, the geometric compatibility factor *m*’ was used to assess the geometric alignment among grains for the activation of different slip systems [42–45]. However, the behavior of slip transfer could only be rationalized partially by geometric criteria due to the neglect of the effect from the variation of the elastic modulus and CRSS. For instance, it is revealed that the plastic anisotropy of hcp materials, which is related to the various CRSS for different slip systems, promotes twinning transmission [36]. It is also found that the elastic and plastic anisotropy of single crystals and strong grain-grain interaction are the main factors for the surprising phenomenon that the stress along the loading axis decreases in some grains during tensile test just beyond the macroscopic yield point [46].

In this study, an excellent combination of the strength of fine-grain layers and the ductility of coarse-grain layers is achieved in the specially designed C/F-Ti. The focus of this paper is to investigate the cause of the extraordinary strengthening in C/F-Ti by advanced characterization and in-depth analysis. Synchrotron Laue X-ray microdiffraction is selected to characterize the evolution of lattice strain distribution during in-situ tensile test due to its good angular resolution (~0.01°) and deviatoric strain revolution (~10^{-4}). Different slip systems activated at different domain areas are analyzed by transmission electron microscopy (TEM). It is found that the outstanding strengthening of C/F-Ti primarily relies on the texture, the constraint of strain transfer between neighboring layers and the large difference in the CRSS of different slip/twinning modes in titanium. These findings provide new opportunities to design better microstructures and mechanical properties of hcp metals.

Table 1
Chemical composition of CP Ti.

Elements	Ti	Fe	O	C	H	N
Content (wt.%)	Bal.	0.030	0.050	0.011	0.003	<0.008

2. Experimental

2.1. Materials

Commercial pure titanium (CP Ti) sheets with thicknesses of 100 μm and 20 μm produced by cold rolling and annealing were used as starting material. The chemical composition of CP Ti is given in Table 1. The Ti sheets were cut into about 100 × 100 mm^2 in size. Annealing was carried out for Ti sheets with a thickness of 100 μm at 700°C for 2 h in vacuum to obtain coarse grains. Both the Ti sheets with a thickness of 100 μm and a thickness of 20 μm were eroded using 10 vol.% HF solution in order to remove the oxide layers on the surfaces. Then the Ti sheets of about 92 μm and 12 μm were stacked alternatively to form a 3 mm thick sample. Finally, the layered titanium with alternating coarse- and fine-grain layers (C/F-Ti) was fabricated by hot-pressing at 700°C for 2 h in vacuum under a pressure of 40 MPa to bond the sheets. For comparison, layered titanium samples of only coarse-grain layers(C-Ti) and only fine-grain layers (F-Ti) were also fabricated from the same sheets in the same manner.

The microstructures of the samples were characterized in the section containing the initial rolling direction (RD) and normal direction (ND) by HKL electron backscatter diffraction (EBSD) with a scanning electron microscope (SEM, ZEISS MERLIN COMPACT). The specimens were electrochemically polished in a solution composed of 5 ml perchloric acid, 35 ml n-butanol and 60 ml methanol. EBSD mapping was carried out at an acceleration voltage of 20 kV with a step size of 2 μm for C-Ti and C/F-Ti, and 1.2 μm for F-Ti samples.

2.2. Mechanical tests

Tensile tests were performed for C-Ti, F-Ti and C/F-Ti samples. Dog-bone shaped tensile specimens with a gauge length of 18 mm and a width of 5 mm were cut by electron discharge machining such that the tensile direction was parallel to the RD. The tensile tests were carried out at a strain rate of 10^{-3} s^{-1} at room temperature using an Instron-1186 Universal Testing Machine. Three specimens were tested for each condition and in total nine tests were done.

The hardness distribution across the layer was determined by nanoindentation tests using a Nano-Indenter XP machine. The specimens were prepared by electrochemical polishing on the RD-ND section. Nano-indents with a spacing of 10 μm along the ND were made to a maximum depth of 1 μm. The microstructure of the area tested by nanoindentation was characterized by EBSD with a step size of 1.5 μm in the SEM.

2.3. Lattice strain evolution obtained by μXRD

In-situ synchrotron Laue X-ray microdiffraction (μXRD) at different applied stress during tensile test a strain rate of 10^{-3} s^{-1} was carried out on Beamline 12.3.2 at the Advanced Light Source (ALS) in Lawrence Berkeley National Laboratory (LBNL) [47]. A C/F-Ti tensile sample with gauge dimensions of 12 mm long, 1 mm wide and 0.5 mm thick was cut with the tensile direction parallel to the RD. The sample for μXRD was polished in the same way as that for EBSD. In-situ collection of Laue patterns was carried out using an X-ray beam with an energy bandpass of 5-24 keV parallel to the layer interface approximately at the center of the RD-ND section during the tensile test. The sample was mounted on an X-Y scanning stage with a tilt angle of 45° relative to the incident X-ray beam. The X and Y scanning directions are parallel to the ND and RD of the sample, respectively. A focused white beam of about 1×1 μm^2 and a scanning step size of 2 μm were used. The Laue diffraction data were analyzed through a custom-developed software called XMAS in order to obtain information about the distribution of crystal orientation, lattice strain, etc [48] and visualized by a software package called XtalCAMP [49]. The experimental setup and the data analysis provided an angular resolution up to 0.01° (in consequence, a deviatoric strain resolution of 10^{-4}) [50]. Different dislocation types could be suggested by various shapes of diffraction peaks [51–54].

2.4. TEM observation of dislocation structures

TEM (JEOL JEM2100 operated at 200 kV) was used to analyze the dislocations activated in individual grains in the tensile samples deformed to a plastic strain of 0.15%. Thin foils for TEM observations were cut out from the uniform gauge section of the tested samples and then prepared by grinding and electropolishing using a modified window technique [55].

3. Results

3.1. Layered microstructures

The microstructures of the as-processed layered titanium samples before the tensile test are shown in Fig. 1. The inverse pole figure (IPF) coloring maps (transverse direction, TD) of C-Ti, C/F-Ti and F-Ti samples obtained by EBSD (Fig. 1a–c) indicate that the layer interfaces are general straight and continuous. Some grains grow into the neighboring layers, indicating a good layer bonding. No particles or pores are observed at the layer interface. C-Ti and F-Ti samples consist of layers with uniform coarse grains and fine grains, respectively, while C/F-Ti is composed of alternating coarse- and fine-grain layers.

The average grain sizes were measured by the line-intercept method, showing that the average grain size (mean chord length) of C-Ti (47.8 μm) is similar to that of the coarse-grain layers in C/F-Ti (50.2 μm) while the average grain size of F-Ti (9.2 μm) is similar to that of the fine-grain layers of C/F-Ti (9.8 μm). Note that for both the C-Ti sample and the coarse-grain layers in the C/F-Ti sample, many grains have their sizes matching the layer thickness although the average grain size is about half of the coarse-grain layer thickness. Such a matching of the grain size with the layer thickness is obvious for the fine-grain layers. Such a relation between the grain size and the layer thickness provides a circumstance where the layer interfaces will impose a strong constraint effect on the deformation of grains. The textures of the three samples are similar—all exhibiting a strong split basal texture with the normal of the basal planes tilted away from ND towards TD with peaks at about ±30° (shown in Fig. 1d–g, respectively), similar to textures of Ti reported in other work [32,33,56].

3.2. Mechanical properties

3.2.1. Tensile properties

Tensile engineering stress-strain curves of layered titanium (C-Ti, C/F-Ti and F-Ti) are shown in Fig. 2a. C/F-Ti exhibits a yield strength ($\sigma_{0.2}$) of 212 MPa, which is nearly the same as that of F-Ti (214 MPa). At the same time, the elongation to failure (ε_f) of C/F-Ti is 53%, which is higher than that of F-Ti (42%). The uniform elongation (ε_u) of C/F-Ti is 18%, which is between the values for C-Ti and F-Ti. The strain hardening rate (θ=dσ/dε) versus true strain curves are plotted in Fig. 2b. To a true strain of 12%, the strain hardening rate of C/F-Ti is lower than that of F-Ti but higher than that of C-Ti. Afterwards, the hardening rate of F-Ti becomes the lowest among the three samples, while the hardening rate of C-Ti and C/F-Ti are close to each other. The values of mechanical properties are shown in Table 2.

C/F-Ti contains a large volume fraction (89.3%) of coarse grains, but its strength is much higher than that of C-Ti, indicating extra hardening to the coarse grains in C/F-Ti caused by the special layered design. In the following, the focus is therefore on the characterization of deformation behavior of the coarse-grain layers of C/F-Ti.

3.2.2. The distribution of hardness

An IPF coloring map of the area after nanoindentation tests is shown in Fig. 3a. The distribution of hardness across the layer interface in C/F-Ti is displayed in Fig. 3b. The hardness near the layer at the positions with a distance from 0 to 10 μm to a layer interface is much higher than that (1.81 GPa) at the positions with a distance from 40 to 50 μm to a layer interface. The farther away from the layer interface, the lower the hardness is. No gradient of dislocation density is seen across the interface in the starting hot-pressed C/F-Ti, supported by the EBSD results on local misorientation distribution (Fig. S1 of supplementary), indicating that the measured hardness gradient is not caused by the initial distribution of dislocations.

The crystal orientation has some influence on the hardness. The c-axis of grain 3 (g3) is closer to the TD compared to that of grain 4 (g4). Consequently, the hardness of grain 3 is higher than that of grain 4. The hardness at a position of 46 μm from the layer interface in grain 3 (along line 4) is 2.04 GPa, which is 0.28 GPa higher than that at the same distance to the interface in grain 4 (along line 6). However, most of the grains have their c-axes approximately 60° inclined to the TD caused the split basal texture, and therefore the influence of orientation on the hardness is much smaller compared to that of the layer interface.

To compare the effect of grain boundaries and layer interfaces on the hardness, grain 1 and 2 (marked as g1 and g2 in Fig. 3a) are selected because the nanoindentation for these grains were carried out both at their grain boundaries and in the interior. The hardness values of indents along the lower part of line 1 and line 2 in grain 1 and along the lower part of line 5 in grain 2 are plotted in Fig. 3c. The average hardness values at the grain boundary region and the interior of grain 1 are 1.83 GPa and 1.75 GPa, respectively, while the hardness at the position 10 μm to the layer interface is 2.25 GPa, much higher than that at the grain boundary region. The same trend occurs in grain 2, where the average hardness is 1.98 GPa and 1.88 GPa for the grain boundary region and the interior, respectively, much lower than 3.17 GPa measured next to the layer interface.

3.3. Local strain analyses at different stress levels

3.3.1. The distribution of lattice strain

The evolution of lattice strain in a grain (grain A) of the coarse-grain layer in C/F-Ti (Fig. 4f) during the in-situ tensile test is

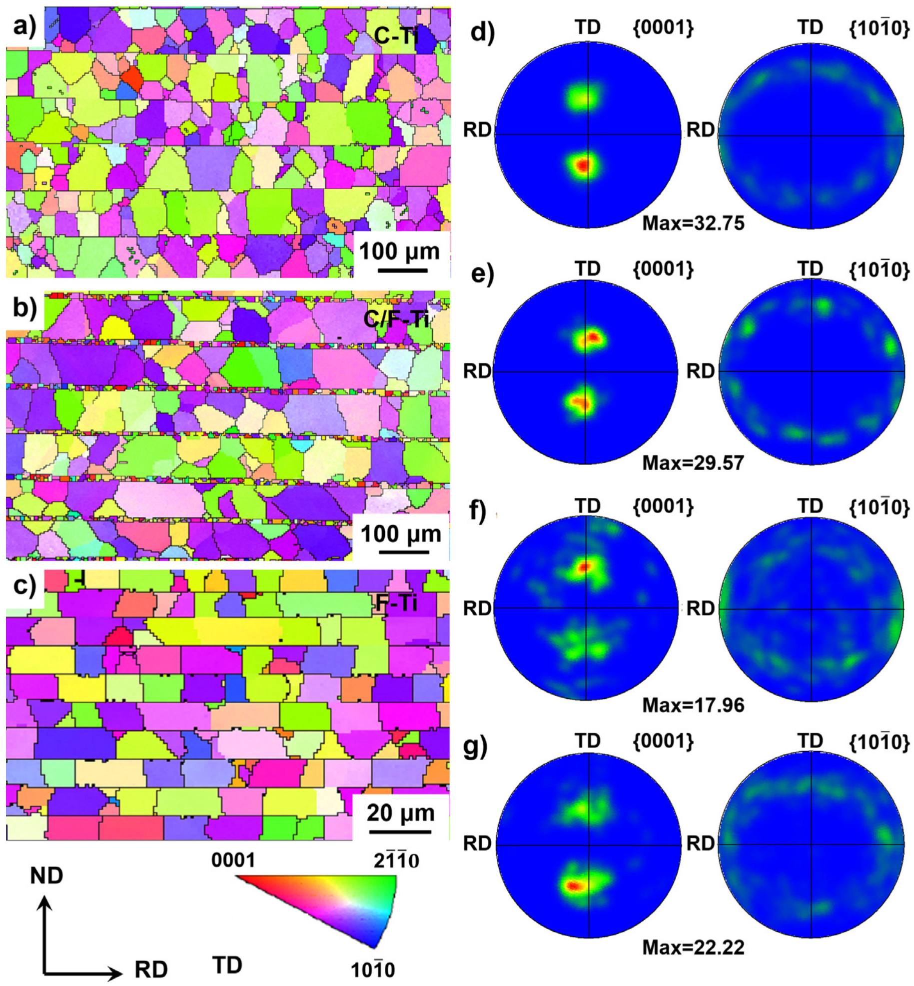

Fig. 1. Microstructure of layered titanium: IPF coloring maps (TD) in the RD-ND section of (a) C-Ti; (b) C/F-Ti; (c) F-Ti; the pole figures of C-Ti, coarse-grain layers of C/F-Ti, fine-grain layers of C/F-Ti and F-Ti are shown in (d); (e); (f); (g), respectively.

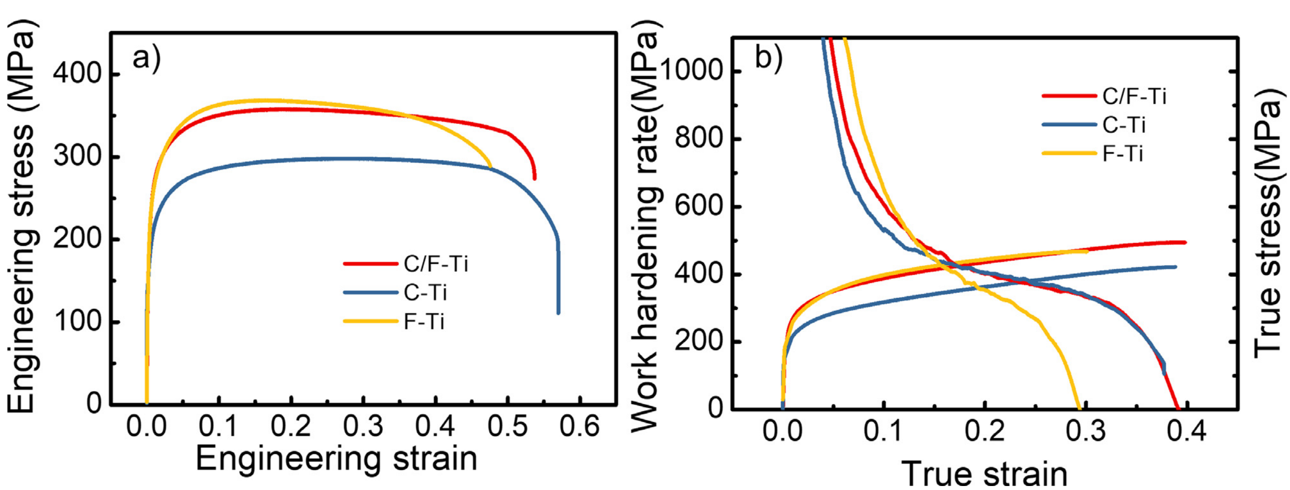

Fig. 2. (a) Tensile engineering stress-strain curves; (b) work hardening rate (θ=dσ/dε) and true stress verses true strain curves.

Table 2
Mechanical properties of C-Ti, C/F-Ti and F-Ti.

Mechanical properties	Yield strength $\sigma_{0.2}$ (MPa)	Uniform elongation ε_u (%)	Fracture elongation ε_f (%)	Tensile strength σ_s (MPa)
C-Ti	161±4	24 ± 1	54 ± 2	292 ± 4
C/F-Ti	212±6	18±1	53±2	354±4
F-Ti	214±4	15±1	42 ± 6	365 ± 3

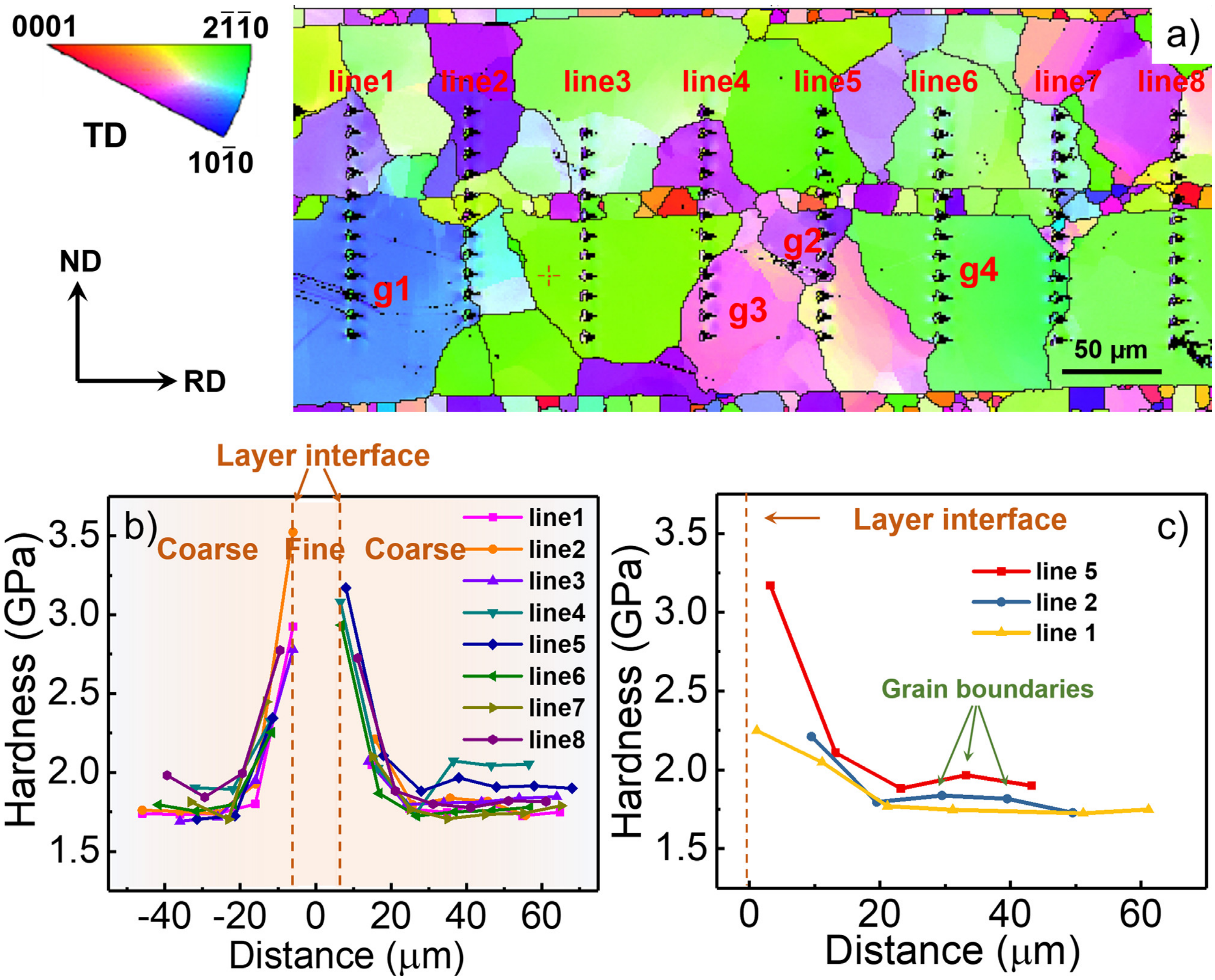

Fig. 3. Nanoindentation test on C/F-Ti. (a) IPF coloring map with 8 testing lines and 6 grains indicated; (b) hardness versus distance to the layer interfaces curves; (c) comparison among the hardness values of grain boundary region, grain interior and layer interface region in grain 1 and grain 2, corresponding to the lower part of nano-indents of line 1, line 2 and line 5.

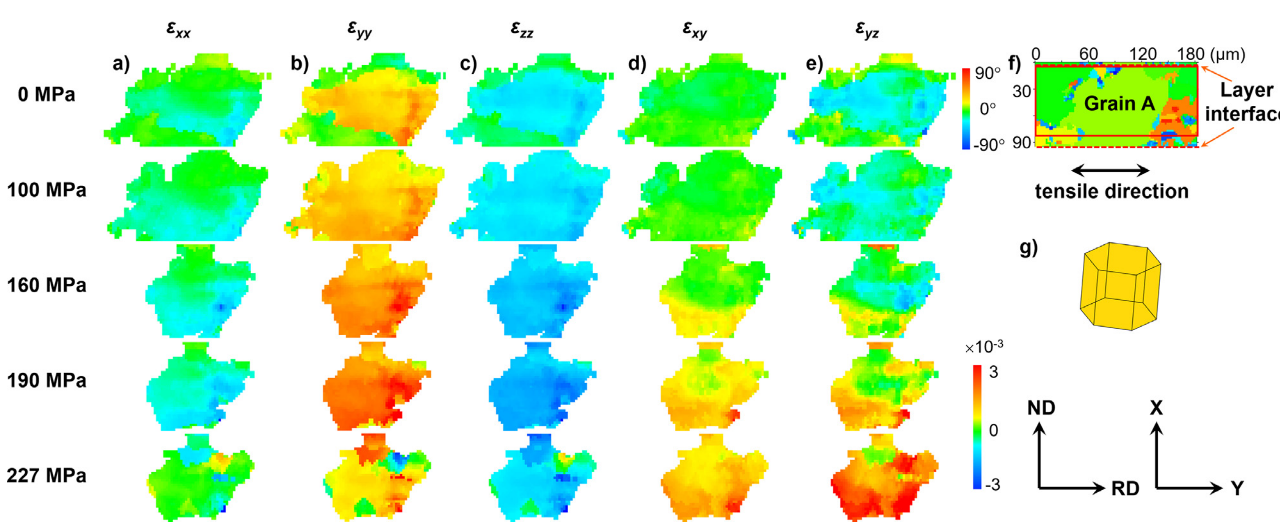

Fig. 4. The evolution of the deviatoric strain tensor: (a) ε_{xx}, (b) ε_{yy}, (c) ε_{zz}, (d) ε_{xy}, (e) ε_{yz} at different tensile stress levels: 0 MPa, 100 MPa, 160 MPa, 190 MPa and 227 MPa in grain A; (f) Euler angle (ϕ_1) map of grain A; (g) The orientation schematic diagram of grain A.

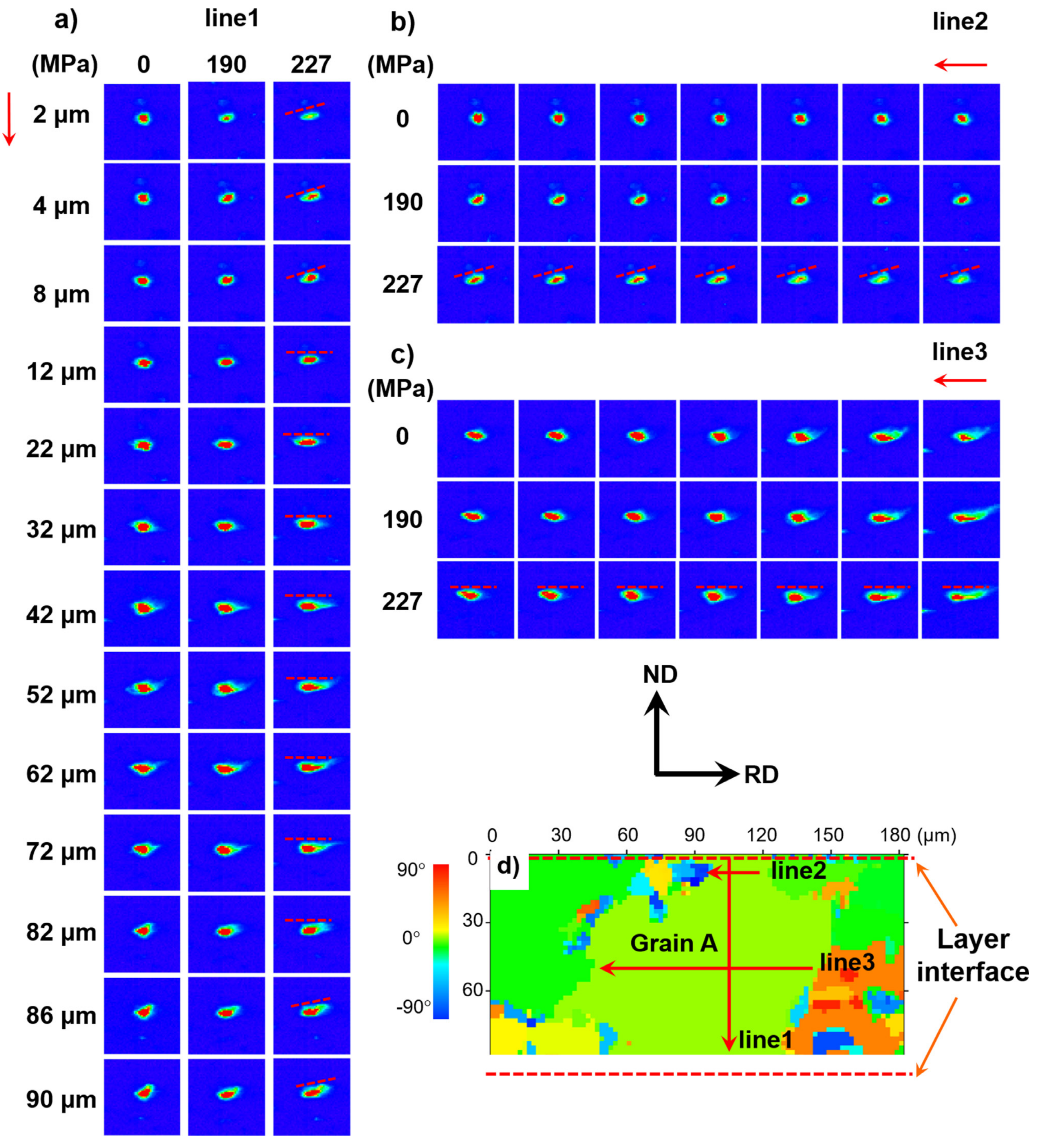

Fig. 5. The evolution of peak shapes at various positions along the orange lines in grain A during tensile test. (a) Line 1, (b) line 2, (c) line 3, (d) Euler angle (ϕ_1) map of grain A.

obtained by Synchrotron Laue X-ray microdiffraction. Due to the strong split basal texture and the narrow grain size distribution in C/F-Ti, grain A with typical size and orientation as shown in Fig. 4g is selected as an example to analyze the strain evolution of coarse grains in C/F-Ti, focusing on the differences between regions next to the layer interface and in the layer center. The distribution of five components of lattice strain tensor at different tensile stress (0 MPa, 100 MPa, 160 MPa, 190 MPa and 227 MPa) are shown in Fig. 4 (note that lattice strain shown in this paper is deviatoric lattice strain different from full strain, but the relative magnitude at different tensile stress is comparable within a grain). The diffraction spots of grain A (Fig. 5) is relatively round, which indicates that the calculated deviatoric strain is quite reliable. When the applied stress increases to 160MPa, the indexing of diffraction spots of the area near the left grain boundary becomes unsuccessful, which may be due to relatively large lattice rotation in this area. It is found that the residual strain is distributed heterogeneously inside grain A in the initial state and it is about 10^{-3} along the tensile direction (ε_{yy}). As the tensile strain increases to 100 MPa, the distribution of local strain component ε_{yy} becomes more homogeneous due to the superimposition of residual stress and applied stress along the tensile direction, and the ε_{zz} component (along the TD) and ε_{xx} component (along ND) shows an increase of compressive strain, in agreement with the Poisson effect. The different increments of the components ε_{xx} and ε_{zz} are related to the elastic anisotropy of Ti [26,57]. The shear strain components do not exhibit significant change during this period of elastic deformation. When the applied stress reaches 160 MPa, there are significant changes in the shear strain components ε_{xy} and ε_{yz} near the layer interface, indicating local yielding through dislocation activities. However, ε_{yy} still increases nearly homogeneously in the grain. This tendency remains at the applied stress of 190 MPa, which approaches the yield stress of C/F-Ti. At the applied stress of 227 MPa, which is higher than the yield stress of C/F-Ti, the lattice strain component ε_{yy} along the tensile direction becomes heterogeneous in the grain. The component ε_{yy} decreases in the interior of the grain while increases continuously near the layer interface. The obtained maximum value of ε_{yy} is 2.73×10^{-3} (corresponding to 245 MPa), which is slightly larger than the global yield stress of C/F-Ti (212 MPa), giving further confidence to the calculated deviatoric strain results.

3.3.2. Analysis of activated slip systems

The diffraction peaks of $(41\bar{5}4)$ are extracted from the Laue patterns in order to analyze the evolution of the peak at different positions in grain A during the tensile test. The peaks along the three orange lines (Fig. 5d) at different tensile stress: 0 MPa, 190 MPa and 227 MPa are displayed in Fig. 5a–c. For each position in line 1, the distances to the top layer interface (Fig. 5d) are shown on the left of Fig. 5a. From peaks of line 1 at a tensile stress of 227 MPa (Fig. 5a), it is found that the peaks extracted from positions near the layer interface (i.e. at the top three and bottom two positions) streak towards a different direction (along red dotted lines) compared to that from the interior of the layer. This is related to the different slip systems activated at different positions of the grain. Various streaking directions of the diffraction peaks in Laue patterns are related to the activation of different slip systems. To confirm this phenomenon, peaks from line 2 extracted every 4 μm along the layer interface and from line 3 extracted every 16 μm along the middle of the layer were also analyzed and are shown in Fig. 5b and c. The peaks from the interface region streak towards the same direction which is different from that of peaks from the middle of the layer.

3.4. Dislocation structure (0.15% plastic strain)

Dislocation structures were observed and analyzed under different diffraction conditions by TEM. In the two areas shown in Fig. 6a and c, which are extracted from the larger area along a layer interface shown in Fig. S2 of Supplementary, many dislocations appear in the coarse-grain layer along the layer interface at a plastic strain of 0.15%. Most of these dislocations are visible when imaged nearly along the $[1\bar{2}10]$ zone axis (Fig. 6a and c) and invisible when imaged with $\mathbf{g} = [0002]$ near the $[1\bar{2}10]$ zone axis (Fig. 6b and d). Therefore, these dislocations have a Burgers vector $\mathbf{b} = \langle\mathbf{a}\rangle$ ($\mathbf{b} = 1/3\langle 1\bar{2}10\rangle$) based on the invisible criterion of $\boldsymbol{g}\cdot\boldsymbol{b} = 0$. Pile-ups of dislocations with $\mathbf{b} = \pm 1/3[11\bar{2}0]$ (supported by Fig. S3a and b of supplementary) and $\mathbf{b} = \pm 1/3[\bar{2}110]$ (supported by Fig. S3c and d of Supplementary) can be observed near the layer interface in Fig. 6a and c (along the orange dotted lines), respectively. Dislocations which are visible in both conditions are considered as <c+a> dislocations with $\mathbf{b} = \langle 2\bar{1}\bar{1}\bar{3}\rangle$. A few <c+a> dislocations with $\mathbf{b} = \pm 1/3[\bar{2}113]$ (pointed by a red arrow) and with $\mathbf{b} = \pm 1/3[\bar{2}11\bar{3}]$ or $\mathbf{b} = \pm 1/3[\bar{2}11\bar{3}]$ (pointed by a green arrow) are observed along the layer interface in Fig. 6b. Meanwhile, twins also appear near the interface (pointed by orange arrows in Fig. 6c and d). In contrast, the TEM images captured towards the interior of the layer show no <c+a> dislocations through imaging with $\mathbf{g} = [0002]$ (shown in Fig. S5 of Supplementary), indicating that <c+a> dislocations mostly appear near the layer interfaces. In order to investigate the effect of grain boundaries within the coarse-grain layer, an area near a grain boundary along the ND is extracted from the same grain, shown in Fig. 7. However, only one short pile-up with a few <a> dislocations with $\mathbf{b} = \pm 1/3[11\bar{2}0]$ (supported by Fig. S4 of Supplementary) is observed and no <c+a> dislocations are observed.

In the fine-grain layers, there are also pile-ups of <a> dislocations (along orange dotted lines) with $\mathbf{b} = \pm 1/3[\bar{2}110]$ (supported by Fig. S6 of Supplementary) near the layer interface as shown in Fig. 8a. In this example, one pile-up of <c+a> dislocations (along red dotted lines) with $\mathbf{b} = \pm 1/3[11\bar{2}\bar{3}]$ or $\mathbf{b} = \pm 1/3[\bar{1}2\bar{1}\bar{3}]$ (supported by Fig. S6 of Supplementary) near the layer interface is also observed in the fine grain—both visible when imaged nearly along the $[11\bar{2}0]$ zone axis and with $\mathbf{g} = [0002]$ near the $[11\bar{2}0]$ zone axis.

4. Discussion

A combination of high yield strength and high elongation has been observed in the layered C/F-Ti, where the layer interface shows a strong influence on the local hardness and deformation mechanisms. The yield strength of layered titanium (C-Ti, C/F-Ti and F-Ti) from this work and non-layered pure titanium with similar chemical compositions from other work [58–60] are compared in Fig. 9. The relationship between yield strength and grain size for the C-Ti, F-Ti and pure titanium largely follow the Hall-Petch relation [61,62], although the slope varies slightly possibly due to the influence of texture. Therefore, layer interfaces in C-Ti and F-Ti do not exert a significant effect on the yield strength. However, the yield strength of C/F-Ti deviates from the Hall-Petch relation dramatically and it is also much higher than that calculated by ROM [16,17]. The underlying mechanism for the enhanced yield strength of C/F-Ti is analyzed with respect to the effects of texture, grain size distribution and layered structure on the deformation mechanism.

4.1. The effect of texture on deformation mechanism

The TEM investigations reveal that <a> slip is the dominant deformation mechanism during tensile deformation of the C/F-Ti sample. Such a deformation pattern is related to the texture of the material. The C/F-Ti has a strong split basal texture with the basal plane normal tilted about ±30° towards the TD as shown in Fig. 1. CRSS and Schmid factors of different slip systems are the main factors influencing the yielding of grains. The average Schmid factors for different slip systems of coarse-grain layers are calculated based on the highest factor for each type of slip systems for each pixel from the EBSD data, shown in Table 3, while the CRSS values of different slip and twinning modes of pure Ti determined by crystal plasticity modeling [25,26,63–65] and measured by experiment [31] are shown in Table 4. The prismatic <a> slip with the lowest CRSS has the highest average Schmid factor among different slip modes. Therefore, prismatic <a> slip is expected to be activated first as in a number of previous studies in a similar loading condition [27,31,35,65].

In polycrystalline materials, the interaction between neighboring grains may also play an important role in determining the deformation mechanism. The geometric compatibility factor m' can be used to assess the possibility of activating dislocation sources in adjacent grains through stress concentration at grain boundaries. The larger the factor m' is, the easier the dislocation source

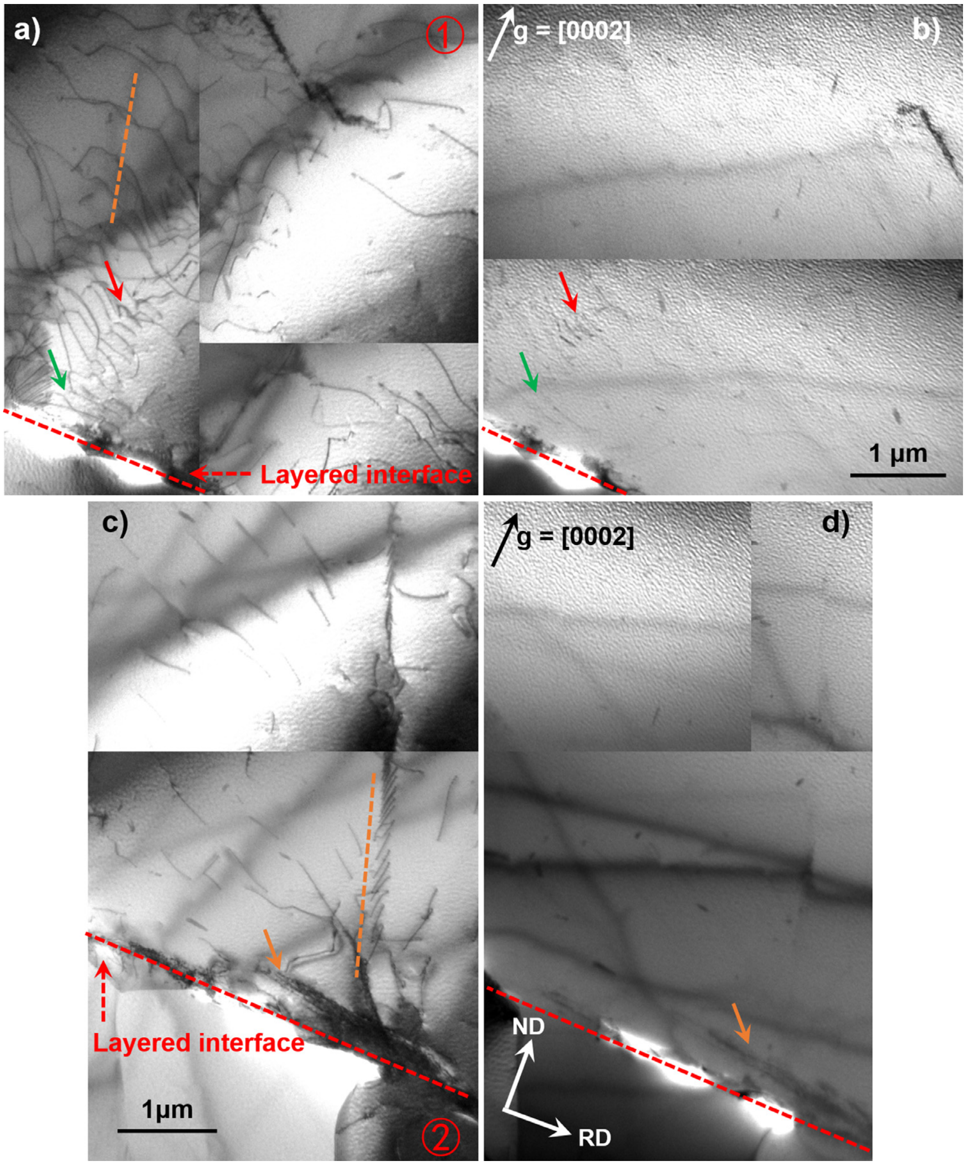

Fig. 6. Bright field (BF) TEM images of two positions in the coarse-grain layer of C/F-Ti near a layer interface at a plastic strain of 0.15%. (a) and (c): the electron beam direction approximately parallel to the $[1\bar{2}10]$ zone axis (**B** $\approx [1\bar{2}10]$); (b) and (d): two-beam BF images using diffraction vector of g = [0002] near the $[1\bar{2}10]$ zone axis. Positions ① and ② are also marked in Fig. S2 of Supplementary.

Table 3
Average Schmid factors of different slip modes under uniaxial tensile test.

Slip modes	Prismatic <a>	Basal <a>	Pyr <a>	Pyr1 <c+a>	Pyr2 <c+a>
Schmid factor	0.469	0.099	0.390	0.468	0.430

is to be activated. The m' value is calculated through the formula: m' = $\cos\alpha\cos\beta$, where α/β represents the angle between the slip planes/directions of two neighboring grains. The factor m' for prismatic slip ($m'_{P\text{-}P}$) of the neighboring grains along RD and ND in C/F-Ti are calculated. It is found that m' of neighboring grains along RD and ND are similar, being 0.749 and 0.729, respectively. According to literature [41], a high Schmid factor and a good alignment (m'>0.7) lead to full slip transfer without stress concentration at the grain boundary between two neighboring grains. From this perspective, slip transfer (prismatic slip) without stress concentration is expected in C/F-Ti, in an agreement with other studies in a similar loading condition [65,66]. In other words, the interaction between grains in C/F-Ti due to its texture does not contribute significantly to the enhancement of the yield strength.

4.2. The effect of grain size distribution on deformation mechanism

The C/F-Ti consists of a large volume fraction (88.5%) of coarse grains and a small fraction (11.5%) of fine grains. The grain sizes and their distributions have a strong effect on the yield strength of a material. The yield strength (σ_s) is commonly related to the average grain size (d) by the Hall-Petch relation: $\sigma_s=\sigma_0+kd^{-1/2}$, where σ_0 is the stress required to initiate dislocation movement (incorporating all strengthening effects except the grain size effect) and k is the Hall-Petch slope [42,61,62]. The value of 0.26 MPa•m$^{1/2}$ for k is calculated based on the yield strength and grain size of C-Ti and F-Ti from this work. This value is similar to those reported in the literature [58–60], as shown in Fig. 9. However, the calculated yield strength of C/F-Ti (175 MPa), based on this k value and the average

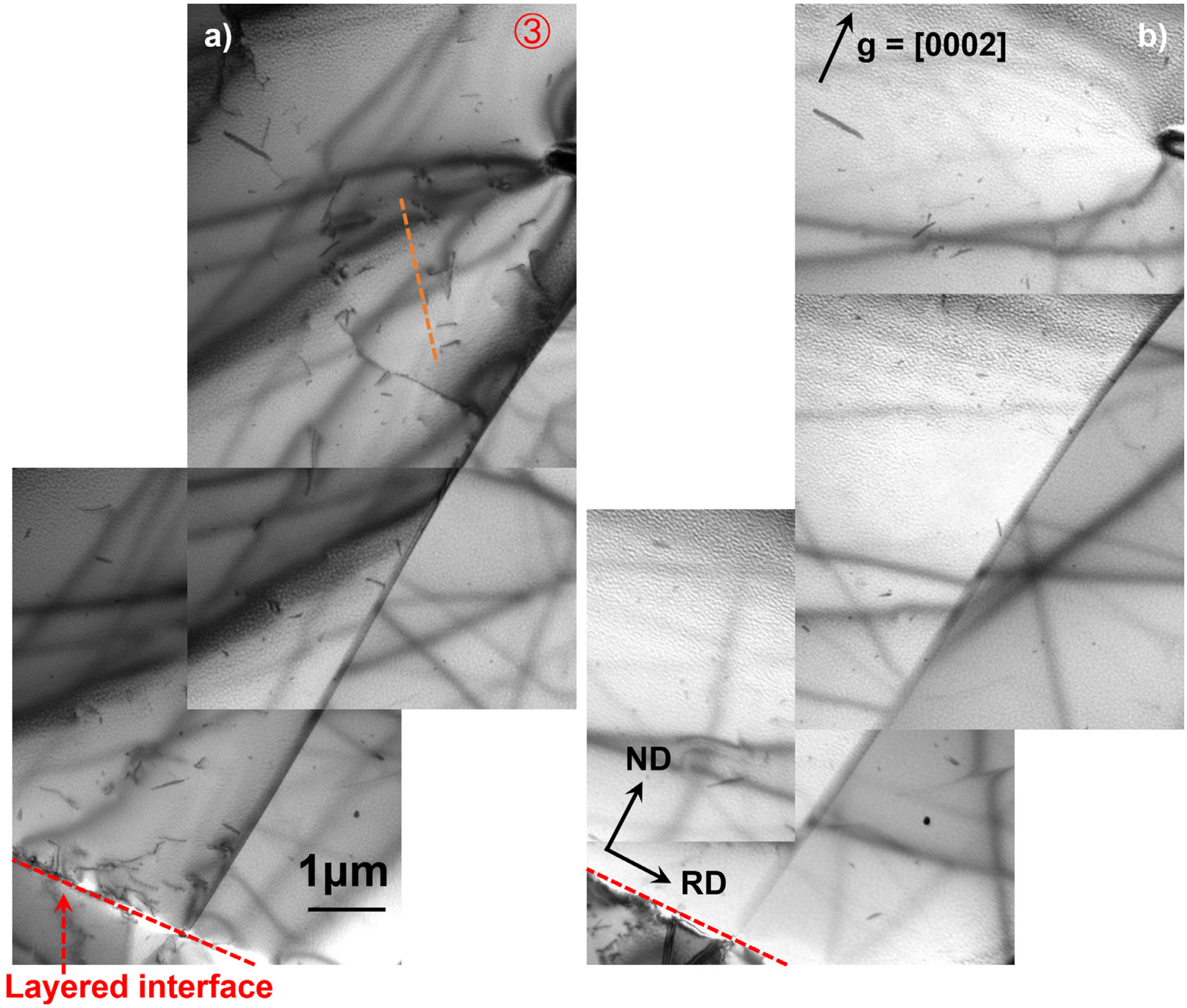

Fig. 7. BF TEM images of an area near a grain boundary, which is perpendicular to the layer interface, in the coarse-grain layer of C/F-Ti at a plastic strain of 0.15%. (a): **B** ≈ $[1\bar{2}10]$; (b): two-beam BF images using diffraction vector of g = [0002] near the $[1\bar{2}10]$ zone axis. Position ③ is also marked in Fig. S5 of Supplementary.

Table 4
CRSS (MPa) values of different slip and twinning modes in pure Ti from references. The oxygen concentration and average grain size are also shown.

Ref.	Prismatic <a>	Basal <a>	Pyr <a>	Pyr <c+a>	Ti twin	O (wt%)	Grain size (μm)
[64]	90	180	140	210	N/A	0.11	9
[26]	80	90	110	260	220	0.06	25
[25]	68	175	120	250	230	0.12	50
[63,65]	60	120	N/A	180	125	0.17	80
[31]	96±18	127 ± 33	N/A	≥ 240	225	0.17	100

grain size directly measured by the line-intercept method including both the coarse- and fine-grain layers (d=30.4 μm), is much lower than the measured yield strength (Fig. 9). The low estimate from the Hall-Petch relation may be partially due to the neglect of the grain size distribution since only the average grain size is considered in the Hall-Petch equation.

For composite materials with two components, the yield strength may be calculated based on the ROM, which is given as $X = f_A X_A + f_B X_B$, where X, X_A and X_B are the yield strength of the composite and the two components, respectively, and f_A and f_B are the volume fractions of each component [16,17]. If we consider the layered configuration in C/F-Ti and add the strength contributions from the coarse- and fine-grained layers which are 142 MPa and 25 MPa, respectively, (based on the volume fraction and yield strength of C-Ti and F-Ti), the ROM estimated yield strength becomes 167 MPa—even lower than that calculated from the Hall-Petch relation. This is because the average grain size of C/F-Ti measured by the line-intercept method is grain boundary area weighted, whereas the strengthening contribution in the ROM is grain volume weighted. In other words, the Hall-Petch relation relies more on small grains while the ROM relies more on big grains. The ROM is widely used to predict the mechanical properties of sandwich sheet materials. The yield strength of layered materials, such as: Cu/Cu-10Zn [11,67] and Ti/Al layered composites [8,10], agree well with the ROM. For these layered composites, the deformation is divided into three stages: elastic stage, elastic-plastic stage and plas-

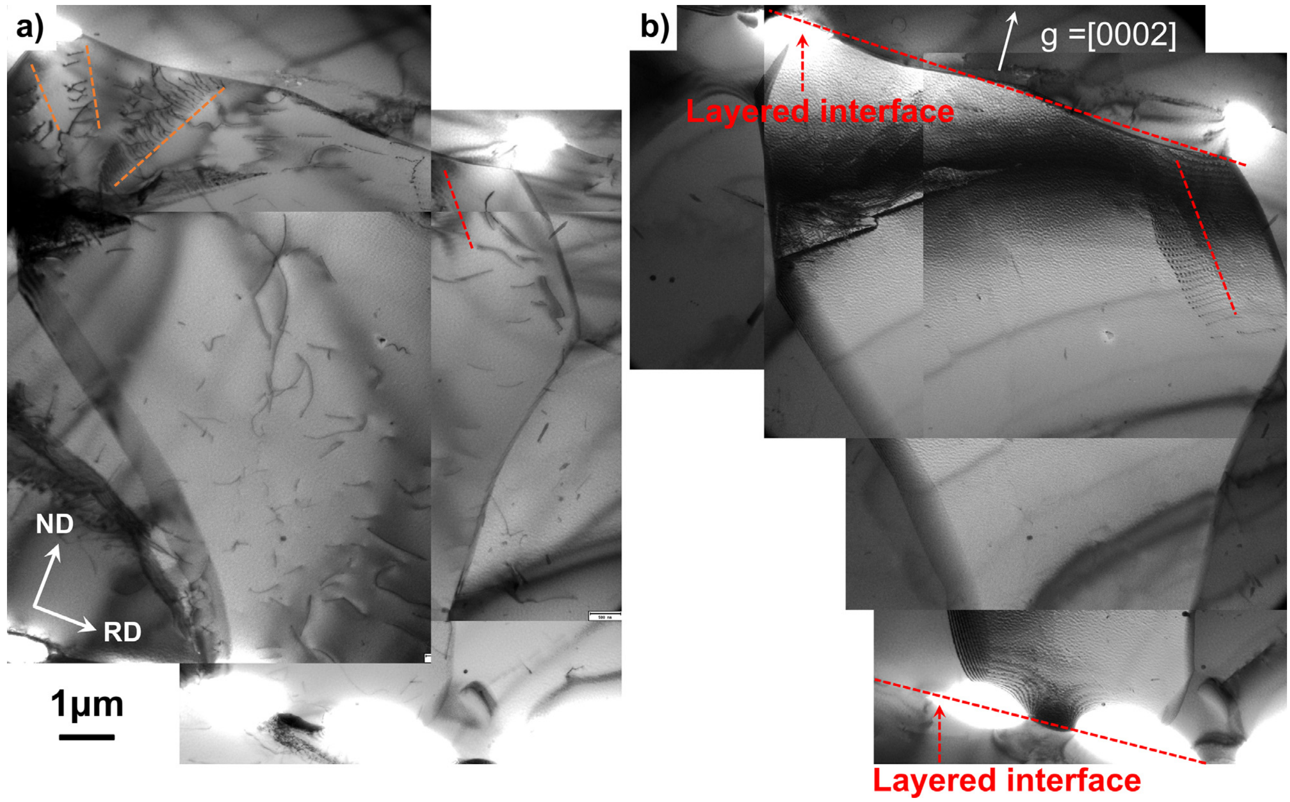

Fig. 8. BF TEM images of the fine-grain layer in C/F-Ti at a plastic strain of 0.15%. (a): **B** ≈ [1$\bar{2}$10]; (b): Two-beam BF images using diffraction vector of **g** = [0002] near the [1$\bar{2}$10] zone axis.

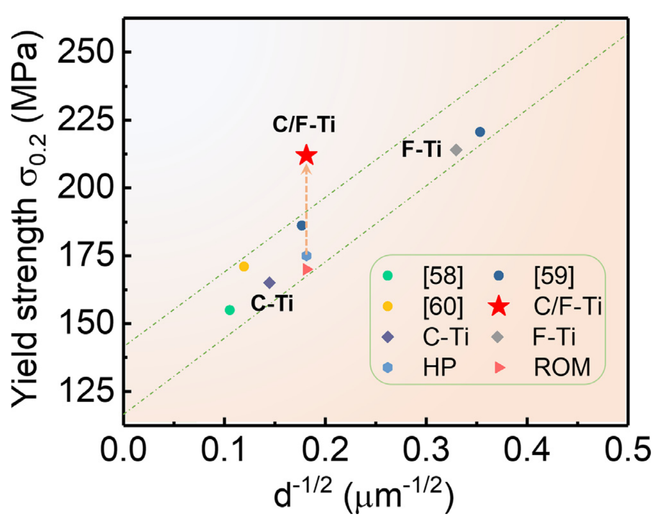

Fig. 9. The relationship of yield strength and grain size (linear intercept values) for the present samples. The data for pure Ti taken from literature [58–60] are also included for comparison.

tic stage. The first two stages are of importance to the macro yielding of the material. Stress partitioning appears at these stages due to the different elastic modulus and yield strength between adjacent layers. Therefore, the yield strength of the composite exhibits a combination of soft layers and hard layers, which obeys the ROM. Nevertheless, the yield strength in the present C/F-Ti does not follow this trend (Fig. 9), indicating a strong interface effect of the layered structure on the deformation mechanism.

4.3. The effect of layered structure on deformation mechanism

In addition to the dominant <a> dislocations, <c+a> dislocations have also been observed near the layer interface in the coarse-grain layers of C/F-Ti at a plastic strain of 0.15%, but not in the interior or the grain boundary areas of the coarse-grain layers (Fig. 7). Moreover, the evolution of the Laue diffraction peak patterns at different strain levels also indicates that different slip systems are activated near the layer interface compared to the interior of the coarse-grain layer (Fig. 5). These microstructural observations are further supported by the nano-indentation results, which show higher hardness next to the layer interfaces (Fig. 3). All these experimental results point to the important role of the interfaces separating coarse- and fine-grain layers in determining the deformation mechanisms and yield strength of C/F-Ti.

It should be mentioned that local residual strain exists in the initial state of C/F-Ti (Fig. 4) probably due to the anisotropy of thermal contraction, resulted from the difference in the thermal expansion coefficient along the <a> and <c> axes of the grains, during cooling after hot pressing. The texture and spatial distribution of grains are similar in C/F-Ti, C-Ti and F-Ti, and therefore the local residual stress is not likely to be a key reason for enhancing the yield strength of C/F-Ti, and will not be discussed further. Hence, the strengthening mechanism of C/F-Ti will be discussed from the perspective of the constraint from the layer interface and the specific deformation behavior of hcp crystalline structure.

4.3.1. The constraint on strain transfer

In order to investigate the strengthening mechanism of C/F-Ti, it is essential to analyze the early stage of deformation. During elastic deformation, both the coarse- and fine-grain layers deform elastically. The stress partitioning, which usually exists in layered composites, is not expected in C/F-Ti due to the same elastic modulus of the two adjacent layers. When the stress increases to 160 MPa during in-situ tensile test, heterogeneous shear strain appears in grain A (Fig. 4d and e), indicating local yielding through activation of dislocations. Given the texture of the coarse grains (Fig. 1) and the possible prismatic <a> slip, the coarse grains cannot deform freely due to the constraint of fine-grained layers as many of the coarse grains are directly constrained on two sides (at least one side) by the neighboring fine-grained layers. No matter which <a> slip is activated, the Burgers vector is constricted on the basal plane, which also produces a strain component along the ND due to the split basal texture. To maintain the interface, the strain component along the ND needs to be accommodated by other deformation modes in coarse grains or deformation of fine grains. However, when <a> slip is activated in some coarse grains, strain transfer to the fine grains is difficult because of the high yield strength of the fine-grain layers. Pile-up of <a> dislocations occurs near the layer interface in the coarse-grain layer of C/F-Ti (Fig. 6) and thus to some extent, produces forward stress to facilitate the activation of dislocation sources in fine-grain layers, as well as other deformation modes in the coarse grains. Back stress is also generated to impede the emission of dislocations from the original <a> slip. When the coarse-grain layers start to yield, the significant changes in the distribution of ε_{xy} and ε_{yz} lattice strain components near the interface and the continuous increase of the normal strain ε_{yy} indicate that the stress state near the layer interface changes from uniaxial stress to multiaxial stress due to the constraint of the layered structure, which directly influences the activation of different slip systems and the applied stress needed to emit dislocations from the original <a> slip. If the dislocation sources of fine grains are not activated when the dislocation sources in coarse grains stop to emit dislocations from the <a> slip, the coarse grains have to activate dislocations from other slip systems to ensure the continuity of the material. However, from the result of in-situ μXRD, the lattice normal strain along the tensile direction increases uniformly in grain A up to an applied stress of 190 MPa (Fig. 4a). In other words, macroscopic yielding does not occur at this stage and the grain primarily deforms through elastic strain even though the applied stress reaches the yield stress of the coarse grains.

4.3.2. Specific deformation behavior of hcp lattice structure

Besides the constraint on strain transfer, the specific deformation mechanisms of the hcp crystal structure also play an important role in enhancing the yield strength of C/F-Ti. For the coarse-grain layers to further deform plastically without strain transfer to the fine-grain layers, more dislocations satisfying the requirement of continuity must be activated to accommodate the strain near the layer interfaces in the coarse-grain layers. For the current C/F-Ti, only <c+a> slip and deformation twinning are able to satisfy the requirement of continuity. The CRSS values of <a+c> slip and twinning are both much higher than that of <a> slip, as shown in Table 4 [31]. As a consequence, the <a+c> slip and twinning can only be activated after a large stress concentration at the layer interface. Since F-Ti and C/F-Ti have a similar yield strength and both <c+a> dislocations and twins are present near the layer interfaces just beyond the yield stress of C/F-Ti, it follows that a similar stress concentration may be required for activation of <c+a> slip and twinning in the coarse-grain layers compared to the activation of <a> slip in fine-grain layers. In short, the necessity of activation of <c+a> slip and/or twinning for strain accommodation and their much higher CRSS values compared to <a> slip significantly increase the yield strength of the coarse-grain layers.

From the perspective of the fine-grain layers, the forward stress from the pile-up of dislocations in coarse grain-layers may only have a limited effect on the yielding of fine grains. The forward stress from the pile-up of <a> dislocations in the coarse-grain layers is primarily along the ND, as the plastic strain in the coarse-grain layers along the tensile direction is compatible with the extra elastic strain in the fine-grain layers with the increase of the external load. Therefore the forward stress from the pile-up of <a> dislocations in the coarse-grain layers may facilitate activation of <c+a> dislocations in the fine-grain layers (a pile-up of <c+a> dislocations is found near the layer interface in the fine-grain layer at the plastic strain of 0.15%, see Fig. 8), but has little effect on the activation of <a> dislocations in the fine-grain layers. In other words, the forward stress has little effect on enhancing the yielding of the fine-grain layers.

5. Conclusions

Layered titanium with alternating coarse- and fine-grain layers (C/F-Ti) was fabricated where most of the grains in individual layers have their sizes matching the layer thicknesses. The mechanical properties were characterized by tensile tests. The yielding behavior in individual layers of C/F-Ti was analyzed based on in-situ lattice strain measurement by Laue X-ray microdiffraction during the early stage of the tensile test (before yielding and just after yielding) and the dislocation structure was characterized by TEM at a plastic strain of 0.15%. The following conclusions are reached:

1) The C/F-Ti combines the strength of fine grains and the ductility of coarse grains. The yield strength of C/F-Ti containing only 11.5% volume fraction of fine grains is 212 MPa, nearly the same as that of fine-grained Ti (214 MPa), and it does not follow either the Hall-Petch relation or the rule of mixture.
2) In the coarse-grain layers, the hardness next to the interface is much higher than that in the layer center. This is related to the different slip systems activated at different positions along the thickness during yielding. At the plastic strain of 0.15%, <c+a> slip and twinning only appear near the layer interface.
3) The high yield strength of the layered C/F-Ti originates from the strong effect of layer interfaces on the deformation mechanism. The initial split basal texture enables activation of <a> slip in the coarse grain layer, but the strong constraint by the hard fine-grain layers inhibits strain transfer from the coarse grain layers to fine grain layers. The pile-ups of <a> dislocations eventually stimulate the <c+a> slip, which has a much higher CRSS than <a> slip, leading to a macro yielding at high stress.
4) The current design of layered coarse- and fine-grain structure to enhance yield strength of Ti is considered to be a general strategy for improving the yield strength of hcp metals with significant differences in the CRSS among different slip/twinning systems.

Declaration of Competing Interest

The authors declare that they have no known competing financial interests or personal relationships that could have appeared to influence the work reported in this paper.

Acknowledgment

This work was financially supported by the National Key Research & Development Program of China (Grant No. 2020YFA0405900, 2017YFB0703103, 2017YFA0403803, 2016YFB0700400), the National Natural Science Foundation of China (Grant No. 51927801, 51971075), Natural Science Foundation of Jiangsu Province (BK20202010) and the European Research Council (ERC) under the European Union's Horizon 2020 research and innovation program (grant agreement No 788567). D. Y. Li would like to acknowledge China Scholarship Council

(No. 201906120182). This research used beamline 12.3.2 of the Advanced Light Source, a DOE Office of Science User Facility under contract no. DE-AC02-05CH11231. The critical comments from Peidong Wu and the assistance from Yao Li are gratefully acknowledged.

Supplementary materials

Supplementary material associated with this article can be found, in the online version, at doi:10.1016/j.actamat.2021.116627.

References

[1] X. Li, K. Lu, Playing with defects in metals, Nat. Mater. 16 (7) (2017) 700–701, doi:10.1038/nmat4929.
[2] K. Lu, The future of metals, Science 328 (5976) (2010) 319–320, doi:10.1126/science.1185866.
[3] R.O. Ritchie, The conflicts between strength and toughness, Nat. Mater. 10 (11) (2011) 817–822, doi:10.1038/nmat3115.
[4] Y. Wei, Y. Li, L. Zhu, Y. Liu, X. Lei, G. Wang, Y. Wu, Z. Mi, J. Liu, H. Wang, H. Gao, Evading the strength-ductility trade-off dilemma in steel through gradient hierarchical nanotwins, Nat. Commun. 5 (2014) 3580, doi:10.1038/ncomms4580.
[5] Z. Li, K.G. Pradeep, Y. Deng, D. Raabe, C.C. Tasan, Metastable high-entropy dual-phase alloys overcome the strength-ductility trade-off, Nature 534 (7606) (2016) 227–230, doi:10.1038/nature17981.
[6] H. Wu, G. Fan, An overview of tailoring strain delocalization for strength-ductility synergy, Prog. Mater Sci. 113 (2020) 100675, doi:10.1016/j.pmatsci.2020.100675.
[7] K. Lu, Stabilizing nanostructures in metals using grain and twin boundary architectures, Nat. Rev. Mater. 1 (5) (2016), doi:10.1038/natrevmats.2016.19.
[8] Y. Du, G. Fan, T. Yu, N. Hansen, L. Geng, X. Huang, Laminated Ti-Al composites: processing, structure and strength, Mater. Sci. Eng. 673 (2016) 572–580, doi:10.1016/j.msea.2016.07.108.
[9] G.H. Fan, Q.W. Wang, Y. Du, L. Geng, W. Hu, X. Zhang, Y.D. Huang, Producing laminated NiAl with bimodal distribution of grain size by solid–liquid reaction treatment, Mater. Sci. Eng. 590 (2014) 318–322, doi:10.1016/j.msea.2013.10.038.
[10] M. Huang, C. Xu, G. Fan, E. Maawad, W. Gan, L. Geng, F. Lin, G. Tang, H. Wu, Y. Du, D. Li, K. Miao, T. Zhang, X. Yang, Y. Xia, G. Cao, H. Kang, T. Wang, T. Xiao, H. Xie, Role of layered structure in ductility improvement of layered Ti-Al metal composite, Acta Mater. 153 (2018) 235–249, doi:10.1016/j.actamat.2018.05.005.
[11] X. Ma, C. Huang, J. Moering, M. Ruppert, H.W. Höppel, M. Göken, J. Narayan, Y. Zhu, Mechanical properties of copper/bronze laminates: role of interfaces, Acta Mater. 116 (2016) 43–52, doi:10.1016/j.actamat.2016.06.023.
[12] T. Nizolek, I.J. Beyerlein, N.A. Mara, J.T. Avallone, T.M. Pollock, Tensile behavior and flow stress anisotropy of accumulative roll bonded Cu-Nb nanolaminates, Appl. Phys. Lett. 108 (5) (2016) 051903, doi:10.1063/1.4941043.
[13] Z. Li, Q. Guo, Z. Li, G. Fan, D.B. Xiong, Y. Su, J. Zhang, D. Zhang, Enhanced mechanical properties of graphene (reduced graphene oxide)/aluminum composites with a bioinspired nanolaminated structure, Nano Lett. 15 (12) (2015) 8077–8083, doi:10.1021/acs.nanolett.5b03492.
[14] M. Goken, H.W. Hoppel, Tailoring nanostructured, graded, and particle-reinforced Al laminates by accumulative roll bonding, Adv. Mater. 23 (22-23) (2011) 2663–2668, doi:10.1002/adma.201100407.
[15] C.X. Huang, Y.F. Wang, X.L. Ma, S. Yin, H.W. Höppel, M. Göken, X.L. Wu, H.J. Gao, Y.T. Zhu, Interface affected zone for optimal strength and ductility in heterogeneous laminate, Mater. Today 21 (7) (2018) 713–719, doi:10.1016/j.mattod.2018.03.006.
[16] D. Lesuer, C. Syn, O. Sherby, J. Wadsworth, J. Lewandowski, W. Hunt, Mechanical behaviour of laminated metal composites, Int. Mater. Rev. 41 (5) (1996) 169–197.
[17] S. Lee, J. Wadsworth, O.D. Sherby, Tensile properties of laminated composites based on ultrahigh carbon steel, J. Compos. Mater. 25 (7) (1991) 842–853, doi:10.1177/002199839102500704.
[18] T. Yu, Y. Du, G. Fan, R. Xu, R. Barabash, N. Hansen, X. Huang, Y. Zhang, In-situ synchrotron X-ray micro-diffraction investigation of ultra-low-strain deformation microstructure in laminated Ti-Al composites, Acta Mater. 202 (2021) 149–158, doi:10.1016/j.actamat.2020.10.050.
[19] P.G. Partridge, The crystallography and deformation modes of hexagonal close-packed metals, Metall. Rev. 12 (1) (1967) 169–194, doi:10.1179/mtlr.1967.12.1.16.
[20] J.C. Williams, M.J. Blackburn, The identification of a non-basal slip vector in titanium and titanium-aluminum alloys, Phys. Status Solidi 25 (1) (1968) K1–K3, doi:10.1002/pssb.19680250146.
[21] M.H. Yoo, Slip, twinning, and fracture in hexagonal close-packed metals, Metall. Trans. A 12 (3) (1981) 409–418, doi:10.1007/BF02648537.
[22] A. Churchman, The slip modes of titanium and the effect of purity on their occurrence during tensile deformation of single crystals, Proceedings of the Royal Society of London. Series A. Math. Phys. Sci. 226(1165) (1954) 216-226. 10.1098/rspa.1954.0250
[23] S. Xu, M. Gong, Y. Jiang, C. Schuman, J.-S. Lecomte, J. Wang, Secondary twin variant selection in four types of double twins in titanium, Acta Mater. 152 (2018) 58–76, doi:10.1016/j.actamat.2018.03.068.
[24] U.F. Kocks, The relation between polycrystal deformation and single-crystal deformation, Metall. Mater. Trans. B 1 (5) (1970) 1121–1143, doi:10.1007/BF02900224.
[25] D. Gloaguen, G. Oum, V. Legrand, J. Fajoui, S. Branchu, Experimental and theoretical studies of intergranular strain in an alpha titanium alloy during plastic deformation, Acta Mater. 61 (15) (2013) 5779–5790, doi:10.1016/j.actamat.2013.06.022.
[26] J.L.W. Warwick, N.G. Jones, K.M. Rahman, D. Dye, Lattice strain evolution during tensile and compressive loading of CP Ti, Acta Mater. 60 (19) (2012) 6720–6731, doi:10.1016/j.actamat.2012.08.042.
[27] L. Wang, Y. Yang, P. Eisenlohr, T.R. Bieler, M.A. Crimp, D.E. Mason, Twin nucleation by slip transfer across grain boundaries in commercial purity titanium, Metall. Mater. Trans. A 41 (2) (2009) 421–430, doi:10.1007/s11661-009-0097-6.
[28] X. Wu, S. Kalidindi, C. Necker, A. Salem, Prediction of crystallographic texture evolution and anisotropic stress–strain curves during large plastic strains in high purity α-titanium using a Taylor-type crystal plasticity model, Acta Mater. 55 (2) (2007) 423–432, doi:10.1016/j.actamat.2006.08.034.
[29] A.A. Salem, S.R. Kalidindi, S.L. Semiatin, Strain hardening due to deformation twinning in α-titanium: constitutive relations and crystal-plasticity modeling, Acta Mater. 53 (12) (2005) 3495–3502, doi:10.1016/j.actamat.2005.04.014.
[30] H. Li, D.E. Mason, T.R. Bieler, C.J. Boehlert, M.A. Crimp, Methodology for estimating the critical resolved shear stress ratios of α-phase Ti using EBSD-based trace analysis, Acta Mater. 61 (20) (2013) 7555–7567, doi:10.1016/j.actamat.2013.08.042.
[31] L. Wang, Z. Zheng, H. Phukan, P. Kenesei, J.S. Park, J. Lind, R.M. Suter, T.R. Bieler, Direct measurement of critical resolved shear stress of prismatic and basal slip in polycrystalline Ti using high energy X-ray diffraction microscopy, Acta Mater. 132 (2017) 598–610, doi:10.1016/j.actamat.2017.05.015.
[32] D. Shechtman, D.G. Brandon, Orientation dependent slip in polycrystalline titanium, J. Mater. Sci. 8 (9) (1973) 1233–1237, doi:10.1007/BF00549337.
[33] S. Mullins, B. Patchett, Deformation microstructures in titanium sheet metal, Metall. Trans. A 12 (5) (1981) 853–863.
[34] K. Sofinowski, M. Šmíd, S. van Petegem, S. Rahimi, T. Connolley, H. van Swygenhoven, In situ characterization of work hardening and springback in grade 2 α-titanium under tensile load, Acta Mater. 181 (2019) 87–98, doi:10.1016/j.actamat.2019.09.039.
[35] X. Xu, D. Lunt, R. Thomas, R.P. Babu, A. Harte, M. Atkinson, J.Q. da Fonseca, M. Preuss, Identification of active slip mode in a hexagonal material by correlative scanning electron microscopy, Acta Mater. 175 (2019) 376–393, doi:10.1016/j.actamat.2019.06.024.
[36] M. Arul Kumar, I.J. Beyerlein, R.J. McCabe, C.N. Tome, Grain neighbour effects on twin transmission in hexagonal close-packed materials, Nat. Commun. 7 (2016) 13826, doi:10.1038/ncomms13826.
[37] H. Abdolvand, A.J. Wilkinson, On the effects of reorientation and shear transfer during twin formation: comparison between high resolution electron backscatter diffraction experiments and a crystal plasticity finite element model, Int. J. Plast. 84 (2016) 160–182, doi:10.1016/j.ijplas.2016.05.006.
[38] F. Xu, R.A. Holt, M.R. Daymond, Modeling lattice strain evolution during uniaxial deformation of textured Zircaloy-2, Acta Mater. 56 (14) (2008) 3672–3687, doi:10.1016/j.actamat.2008.04.019.
[39] Q. Yu, Z.W. Shan, J. Li, X. Huang, L. Xiao, J. Sun, E. Ma, Strong crystal size effect on deformation twinning, Nature 463 (7279) (2010) 335–338, doi:10.1038/nature08692.
[40] Y. M.A. Crimp, Y. Yang, L. Wang, P. Eisenlohr, T.R. Bieler, in: Grain boundary strain transfer and anisotropic polycrystalline deformation in commercial purity titanium, Proceedings of the 12th World Conference on Titanium (Ti-2011), 2012, pp. 1061–1065.
[41] Y. Guo, T.B. Britton, A.J. Wilkinson, Slip band–grain boundary interactions in commercial-purity titanium, Acta Mater. 76 (2014) 1–12, doi:10.1016/j.actamat.2014.05.015.
[42] H. Yu, C. Li, Y. Xin, A. Chapuis, X. Huang, Q. Liu, The mechanism for the high dependence of the Hall-Petch slope for twinning/slip on texture in Mg alloys, Acta Mater. 128 (2017) 313–326, doi:10.1016/j.actamat.2017.02.044.
[43] B. Guan, Y. Xin, X. Huang, P. Wu, Q. Liu, Quantitative prediction of texture effect on Hall–Petch slope for magnesium alloys, Acta Mater. 173 (2019) 142–152, doi:10.1016/j.actamat.2019.05.016.
[44] J. Luster, M.A. Morris, Compatibility of deformation in two-phase Ti-Al alloys: dependence on microstructure and orientation relationships, Metall. Mater. Trans. A 26 (7) (1995) 1745–1756, doi:10.1007/BF02670762.
[45] Z. Shen, R. Wagoner, W. Clark, Dislocation and grain boundary interactions in metals, Acta Metall. 36 (12) (1988) 3231–3242.
[46] H. Abdolvand, J. Wright, A.J. Wilkinson, Strong grain neighbour effects in polycrystals, Nat. Commun. 9 (1) (2018), doi:10.1038/s41467-017-02213-9.
[47] M. Kunz, N. Tamura, K. Chen, A.A. MacDowell, R.S. Celestre, M.M. Church, S. Fakra, E.E. Domning, J.M. Glossinger, J.L. Kirschman, G.Y. Morrison, D.W. Plate, B.V. Smith, T. Warwick, V.V. Yashchuk, H.A. Padmore, E. Ustundag, A dedicated superbend X-ray microdiffraction beamline for materials, geo-, and environmental sciences at the advanced light source, Rev. Sci. Instrum. 80 (3) (2009) 035108, doi:10.1063/1.3096295.
[48] B. Rozaliya, I. Gene, Spatially-resolved local structure and defects, Strain and Dislocation Gradients from Diffraction, World Scientific, 2014.
[49] Y. Li, K. Chen, X. Dang, F. Zhang, N. Tamura, C.-S. Ku, H. Kang, H.-R. Wenk, XtalCAMP: a comprehensive program for the analysis and visualization of scanning Laue X-ray micro-/nanodiffraction data, J. Appl. Crystallogr. 53 (5) (2020) 1392–1403, doi:10.1107/s1600576720010882.

[50] K. Chen, M. Kunz, N. Tamura, H.-R. Wenk, Residual stress preserved in quartz from the San Andreas Fault Observatory at Depth, Geology 43 (3) (2015) 219–222, doi:10.1130/g36443.1.
[51] K. Chen, N. Tamura, B.C. Valek, K.N. Tu, Plastic deformation in Al (Cu) interconnects stressed by electromigration and studied by synchrotron polychromatic X-ray microdiffraction, J. Appl. Phys. 104 (1) (2008) 013513, doi:10.1063/1.2952073.
[52] A. Lupinacci, K. Chen, Y. Li, M. Kunz, Z. Jiao, G.S. Was, M.D. Abad, A.M. Minor, P. Hosemann, Characterization of ion beam irradiated 304 stainless steel utilizing nanoindentation and Laue microdiffraction, J. Nucl. Mater. 458 (2015) 70–76, doi:10.1016/j.jnucmat.2014.11.050.
[53] J. Kou, K. Chen, N. Tamura, A peak position comparison method for high-speed quantitative Laue microdiffraction data processing, Scr. Mater. 143 (2018) 49–53, doi:10.1016/j.scriptamat.2017.09.005.
[54] L. Wang, R. Barabash, T. Bieler, W. Liu, P. Eisenlohr, Study of {11-21} twinning in α-Ti by EBSD and Laue microdiffraction, Metall. Mater. Trans. A 44 (8) (2013) 3664–3674, doi:10.1007/s11661-013-1714-y.
[55] G. Christiansen, J.R. Bowen, J. Lindbo, Electrolytic preparation of metallic thin foils with large electron-transparent regions, Mater. Charact. 49 (4) (2002) 331–335, doi:10.1016/s1044-5803(03)00032-9.
[56] N.P. Gurao, S. Sethuraman, S. Suwas, Evolution of texture and microstructure in commercially pure titanium with change in strain path during rolling, Metall. Mater. Trans. A 44 (3) (2012) 1497–1507, doi:10.1007/s11661-012-1484-y.
[57] T.R. Bieler, L. Wang, A.J. Beaudoin, P. Kenesei, U. Lienert, In situ characterization of twin nucleation in pure Ti using 3D-XRD, Metall. Mater. Trans. A 45 (1) (2013) 109–122, doi:10.1007/s11661-013-2082-3.
[58] H. Alkhazraji, E. El-Danaf, M. Wollmann, L. Wagner, Enhanced fatigue strength of commercially pure Ti processed by rotary swaging, Adv. Mater. Sci. Eng. 2015 (2015) 1–12, doi:10.1155/2015/301837.
[59] R.F. Bunshah, R.S. Juntz, Influence of condensation temperature on microstructure and tensile properties of titanium sheet produced by high-rate physical vapor deposition process, Metall. Trans. 4 (1) (1973) 21–26, doi:10.1007/BF02649600.
[60] N. Srinivasan, R. Velmurugan, R. Kumar, S.K. Singh, B. Pant, Deformation behavior of commercially pure (CP) titanium under equi-biaxial tension, Mater. Sci. Eng. 674 (2016) 540–551, doi:10.1016/j.msea.2016.08.018.
[61] N. Petch, The cleavage strength of polycrystals, J. Iron Steel Inst. 174 (1953) 25–28.
[62] E.O. Hall, The deformation and ageing of mild steel: III discussion of results, Proc. Phys. Soc. Lond. Sect. B 64 (9) (1951) 747–753, doi:10.1088/0370-1301/64/9/303.
[63] Y. Yang, L. Wang, T.R. Bieler, P. Eisenlohr, M.A. Crimp, Quantitative atomic force microscopy characterization and crystal plasticity finite element modeling of heterogeneous deformation in commercial purity Titanium, Metall. Mater. Trans. 42 (3) (2010) 636–644, doi:10.1007/s11661-010-0475-0.
[64] K.E.K. Amouzou, T. Richeton, A. Roth, M.A. Lebyodkin, T.A. Lebedkina, Micromechanical modeling of hardening mechanisms in commercially pure α-titanium in tensile condition, Int. J. Plast. 80 (2016) 222–240, doi:10.1016/j.ijplas.2015.09.008.
[65] L. Wang, R.I. Barabash, Y. Yang, T.R. Bieler, M.A. Crimp, P. Eisenlohr, W. Liu, G.E. Ice, Experimental characterization and crystal plasticity modeling of heterogeneous deformation in polycrystalline α-Ti, Metall. Mater. Trans. A 42 (3) (2010) 626–635, doi:10.1007/s11661-010-0249-8.
[66] M.A. Crimp, Y. Yang, L. Wang, P. Eisenlohr, T.R. Bieler, Grain boundary strain transfer and anisotropic polycrystalline deformation in commercial purity titanium, Proceedings of the 12th World Conference on Titanium (Ti-2011), 2012, pp. 1061-1065.
[67] X.L. Ma, C.X. Huang, W.Z. Xu, H. Zhou, X.L. Wu, Y.T. Zhu, Strain hardening and ductility in a coarse-grain/nanostructure laminate material, Scr. Mater. 103 (2015) 57–60, doi:10.1016/j.scriptamat.2015.03.006.